Revealing the Structure of Stereociliary Actin by X-ray Nanoimaging

Valeria Piazza,[†] Britta Weinhausen,[†,#] Ana Diaz,[‡] Christian Dammann,[†] Christian Maurer,[†] Michael Reynolds,[§] Manfred Burghammer,[§,⊥] and Sarah Köster*[,†,∥]

[†]Institute for X-ray Physics, Georg-August-University Göttingen, Göttingen, Germany, [‡]Paul Scherrer Institute, Villigen, Switzerland, [§]European Synchrotron Radiation Facility, Grenoble, France, [⊥]Department of Analytical Chemistry, Ghent University, Ghent, Belgium, and [∥]Center for Nanoscale Microscopy and Molecular Physiology of the Brain (CNMPB), Göttingen, Germany. [#]Present address: European Synchrotron Radiation Facility, Grenoble, France.

ABSTRACT Hair cell stereocilia are crucial for hearing and the sense of balance. They include an array of accurately packed, parallel actin filaments and act as levers, which transform mechanical deformation into neuronal signals. The length of vestibular stereocilia reaches several micrometers, whereas, for individual microfilaments, the diameter and therefore the characteristic length scale in the lateral direction is on the order of a few nanometers. These orders of magnitude render X-rays an ideal tool for investigating actin packing, and numerous studies on reconstituted *in vitro* systems have revealed important information. Here we report on the characterization of intact stereocilia using two nanoscale X-ray techniques. We use X-ray ptychography to image stereocilia with quantitative phase contrast and high dose efficiency, showing stereocilia with diameters and lengths in the expected range. We further employ X-ray nanodiffraction using a nanofocused X-ray beam on the same order of magnitude as the width of a stereocilium. Despite the small probe volume we can clearly visualize the stereocilia bundles. From the individual diffraction patterns we determine the local orientation of the actin structures and can clearly correlate them with the corresponding visible-light fluorescence images. Furthermore, azimuthal integration of individual diffraction patterns reveals distinct intensity curves, showing modulations of the signal, which reflect the relevant length scales and pronounced order in the biological system. The applied techniques are not limited to the studies on stereocilia but have the potential of being applied to many biological and soft-matter systems, in particular if a pronounced degree of order is present.

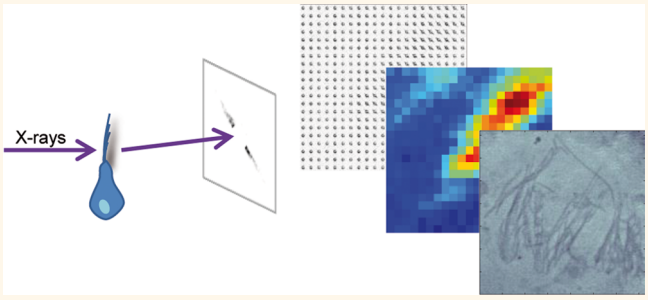

KEYWORDS: vestibular sensory hair cells · stereocilia · actin bundles · nanostructure · X-ray diffraction · ptychography · nanofocused beam

The actin cytoskeleton provides cells with important mechanical and dynamic properties including the ability to firmly grab to surrounding tissue, migrate through tissue or over surfaces, or propel in fluid media. Actin structures built from globular monomers create cellular contraction and oppose bending. All these properties find their origin in the polymeric nature of filamentous actin (F-actin, diameter 7 nm, length up to several μm) and its dualistic capability to polymerize quickly or to be extremely stable over time depending on the cellular situation.[1]

The encoding of mechanical properties in well-defined nano- and microstructures is a very common theme in biological materials as reviewed in ref 2. However, in the wide range of actin-packing assemblies in cells, the compact array of some thousands of parallel actin filaments, which fills the membrane of mechanosensory stereocilia in vertebrates,[3] is thought to represent by far the largest and most ordered cytoplasmic actin structure in cells with only muscle cells containing comparably large and organized microfilament systems.[4−6] The term "paracrystal", created to define substances with some degree of order in their structure without showing long-range order as true crystals, has been used in biology since the 1970s to describe the actin assemblies found in muscle and in stereocilia of the inner ear, as well as the preparations of Mg^{2+}-precipitated, purified F-actin *in vitro*.[3,7]

One successful approach to understand how actin filaments pack into organized structures is by studying purified *in vitro* assemblies using X-ray diffraction methods. In the absence of bundling agents, actin

* Address corresponcence to sarah.koester@phys.uni-goettingen.de.

Received for review July 26, 2014 and accepted November 21, 2014.

Published online November 21, 2014
10.1021/nn5041526

filaments form close-packed bundles and show a hexagonal lattice perpendicular to the longitudinal direction of the filaments. Usually, actin filaments are composed of 13 monomers per six left-handed turns with a rotation of each monomer by 166°.[8] The 13 monomers with a diameter of 5.5 nm result in a double stranded, right-handed helix with a pitch of 72 nm. However, several studies suggest that F-actin can exist in multiple states as a function of the bound nucleotide, ions, and proteolytic modifcations.[9] Actin filaments have a linear charge density of −1 e/2.5 Å at pH 7. This excess of negative charges leads to a rich behavior of actin superstructures upon addition of positively charged lipids[10] or multivalent cations,[11] depending on both the charge and the size of the ions.[12,13]

Ions or charged lipids may act as nonspecific binding agents for charged filaments like F-actin. Additionally, a large variety of specific actin binding proteins (ABP) exists, and these ABPs trigger an equally large variety of actin superstructures, such as bundles, networks or networks of bundles: Whereas α-actinin condenses F-actin into a square lattice phase,[14] both espin and fascin force the filaments in an "overtwisted" hexagonal lattice with a surface-to-surface distance of ∼5.1 nm and thereby facilitate bundle formation. Both these ABPs are enriched in the parallel bundles in stereocilia of hair cells, together with fimbrin,[15] TRIOBP,[16] and others. Espin is a target of mutations that tune espin−actin interactions and are associated with deafness and vestibular dysfunction.[17] Studies of the viscoelastic properties of actin networks cross-linked by wild-type espin or mutant espin reveal that "deafness mutants" lead to weakened viscoelastic properties.[18] *In vitro* X-ray scattering work on a purified actin−espin system provides detailed information about the positions of the diffraction peaks in *q*-space and therefore the real-space inter-actin spacing and geometric order of the filaments.[19] Espin has a Stokes radius of 3.4 nm, and the maximum packing density is one linker per 3−4 actin monomers, which is considerably higher than the physiological density of 0.05−0.07 linkers per monomer. When espin and fascin are compared with respect to their bundling ability in actin systems, they show the same structural end state and lead to very similar bundles, but the different linker stiffnesses cause different pathways for the bundling.[20] Purdy *et al.* find in their *in vitro* system espin-cross-linked parallel hexagonal actin bundles similar to those found in cochlear hair cell stereocilia.[19] Interestingly, the overtwist, which in turn determines the thickness of the bundles, is insensitive to the espin concentration,[19] and the monodisperse thickness of the bundles is rather determined by the stiffness of the linkers.[21]

Numerous *in vitro* studies on reconstituted systems, only some of which are discussed above, provide important insight into the bundling and cross-linking processes of actin. However, in intact biological systems actin filaments are dynamically influenced by numerous factors simultaneously, like binding proteins, ions, lipids, and steric interactions. Whereas *in vitro* experiments allow us to look at certain aspects of self-assembly, they always approximate the system by a limited number of variables and therefore lead to simplifications. A complementary approach is therefore to study the biological system of interest as assembled *in vivo* and then preserve it as closely as possible to natural conditions during the subsequent preparation steps.

As mentioned above, particularly well-ordered actin assemblies are found in muscle and in stereocilia. Early on, researchers have applied X-ray diffraction to muscle preparations to investigate the fascinating structure and dynamics of contracted and relaxed muscle.[4−6] By contrast, X-ray imaging experiments on purified stereocilia have, to the best of our knowledge, not been performed so far. In part, this is certainly due to the challenging sample preparation, which needs to account for the length scales and fragility of the system while requiring a high degree of purity to obtain a reasonable signal-to-noise ratio. At the same time, such studies could provide important insights into the native, unstained, and unsliced system.

Novel X-ray methods now enable us to directly investigate nanoscale biological assemblies. Here, we combine X-ray ptychography for real-space imaging with quantitative phase contrast with a resolution of about 130 nm and X-ray nanodiffraction to obtain structural information in reciprocal space. Using state-of-the-art X-ray optics, we achieve focal spot sizes on the order of 100 nanometers[22−24] and are therefore able to investigate the *local* sample structure, including direction and degree of orientation of the filaments in the stereocilia. The real-space images derived from ptychography or from nanodiffraction dark field contrast can clearly be correlated with corresponding visible light fluorescence images and provide additional quantitative information not accessible by other methods such as quantitative-phase contrast and structural information.

RESULTS AND DISCUSSION

Precise and reproducible sample preparation is critical for the success of X-ray scattering experiments on biological samples. Most "classical" cell culture substrate materials like plastics or glass are not suitable, since they produce a fairly strong background scattering signal themselves, which tends to overlay the signal of the biological matter and additionally absorb much of the scattered intensity. On the contrary, materials that are traditionally used as substrates in X-ray experiments like Kapton or Mylar foils do not enable adhesion of many cells well enough and need to be either coated with adhesion molecules or

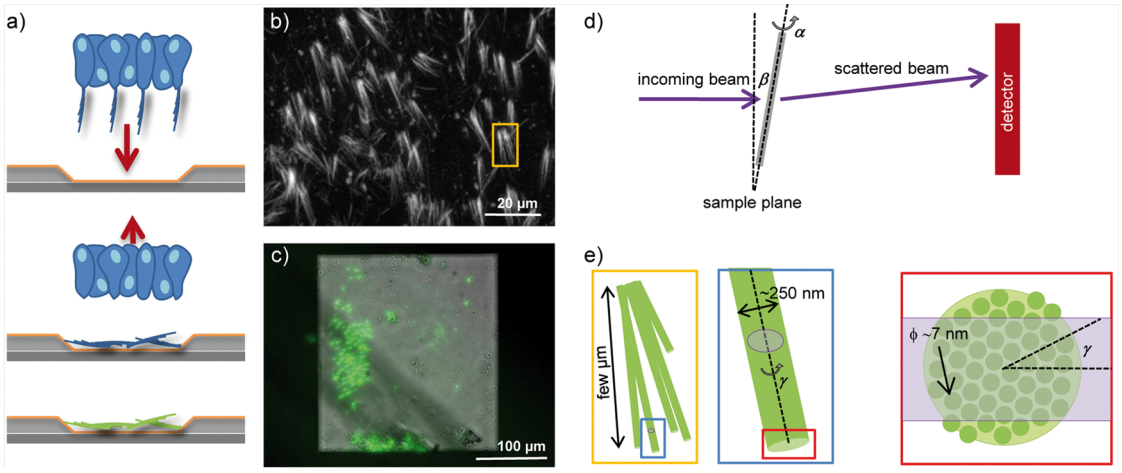

Figure 1. Preparation of stereocilia samples for X-ray experiments. (a) Schematic representation (not to scale) of the blotting of stereocilia onto Si_3N_4 windows. Top: the silicon nitride window is coated with poly-L-ornithine (orange) to promote adhesion of the stereocila bundles. The dissected tissue sample is brought into mechanical contact with the window. Center: when the tissue is removed, the stereocilia remain on the window. Bottom: after fixing and staining for actin with labeled phalloidin the stereocilia can be visualized by fluorescence microscopy. (b) Example of stained stereocilia on a glass coverslip (fluorescence micrograph). (c) Example of stained stereocilia (green) on a Si_3N_4 window (stitched from several individual fluorescence micrographs showing different regions of the window) after lyophilization. (d) Sketched geometry (not to scale) of the setup including the rotation (α) and tilt (β, exaggerated) angles of the sample (thick gray line). (e) Sketch (not to scale) of the hierarchical structure of the sample. The yellow box (see also b) shows a stereocilia bundle; each individual stereocilium is 3−15 μm long. The blue box shows a single stereocilium with a diameter of about 250−300 nm, on the order of the beam diameter (125 × 200 nm^2), and consists of individual actin filaments (red box). Actin filaments are double helices with a diameter of 7 nm and a helical pitch of 72 nm along the filament axis. The structural details are not shown here for simplification. The rotation angle γ of the stereocilia with respect to their long axis is unknown. The approximate beam size for the X-ray nanodiffraction experiments is shown in purple for all three hierarchical levels.

chemically treated to decrease hydrophobicity. Moreover, these materials tend to attract strongly scattering dust particles and debris, which makes identification of the actual biological system on the substrates very difficult. It has been shown that cells can be grown on silicon nitride (Si_3N_4) windows,[25−28] in many cases even without previous coating with an adhesion protein like collagen or fibronectin, and these substrates are furthermore very clean, facilitating the X-ray experiments. A major disadvantage of the windows is their pronounced fragility, which can be accounted for by immersing the substrate in a cell suspension and letting the cells adhere without exerting any mechanical force or stress.

In the case of the experiments reported here, cell fragments instead of whole living cells have to be deposited on the substrate. This aspect makes the sample preparation more challenging since adhesion of cellular parts relies only on the intrinsic, passive adhesiveness of the cell membrane and its constituents and not on the active component represented by the cell adhesion molecules like integrins, selectins and cadherins.[29] To improve this passive adhesiveness, we coat the Si_3N_4 windows with poly-L-ornithine prior to bringing them in contact with the cells. In Figure 1a, top, the Si_3N_4 window (gray) consisting of a thicker frame and a 1 μm thick membrane coated with poly-L-ornithine (orange) is sketched.

Each stereocilium has a diameter of only about 250−300 nm and a length of about 3−15 μm (see Figure 1e for a sketch of the hierarchical structure of the stereocilia). Even though one stereocilia bundle can contain around 60−100 individual stereocilia, the total amount of biological material is very small. In combination with a nanofocused X-ray beam, which is necessary in order to obtain a high spatial resolution in direct space, this leads to a very small probe volume and thus a small number of repeat units. Therefore, very precise and clean sample preparation is critical. By collecting only the stereocilia, not the whole cells, on the Si_3N_4 windows we achieve a situation where actin filaments from the rest of the cell and other cellular components are virtually absent in the preparation, *e.g.*, there is only 1 microtubule-based cilium per bundle of about 60 actin-based stereocilia, and we ensure that the scattering signal we detect indeed arises from the actin filaments in the stereocilia. For the experiments presented here, we employ plunge-frozen, freeze-dried samples. The smaller the sample volume, the more likely it is that during these sample preparation steps the structure remains intact due to enhanced heat dissipation.

The inner ear of young mouse pups was dissected according to standard procedures,[30] and the intact utricle—freed from the otolithic membrane—was carefully separated from the ear. Dissection tweezers were then used to hold the basal part of the utricle so that its top with the protruding stereociliary bundles could be stamped on the surface of the coated Si_3N_4 window (Figure 1a). To ensure that the maximum

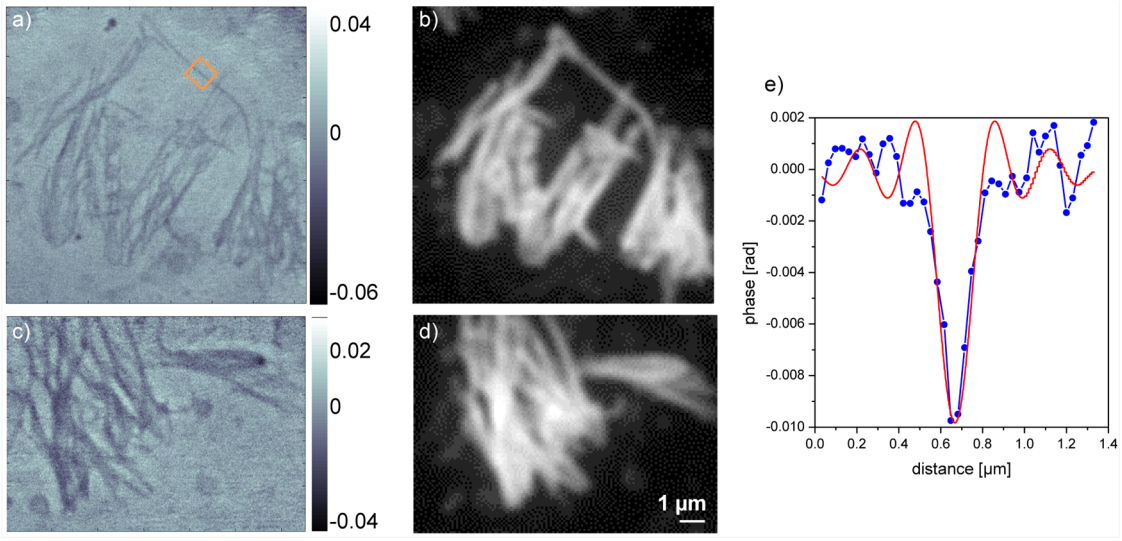

Figure 2. Ptychographic reconstruction of isolated stereocilia, where the grayscale indicates phase in radians. (a, c) Hair cell bundles imaged by ptychography and (b,d) the corresponding fluorescence images taken after the X-ray measurement at 60× magnification. Scale bar is equal for all subfigures. (e) Average phase profile along the stereocilium axis within the orange box in (a); the abscissa represents the distance in the direction perpendicular to this axis; blue line: measurement, red line: simulation of a cylinder of 100 nm diameter convoluted with a sinc function of 130 nm resolution; fwhm of the bundle is 145 (± 15) nm.

number of bundles was collected, the stamping of the utricle was repeated two to three times on different regions of the Si_3N_4 window. This procedure makes certain that the stereocilia are positioned flat on the substrate and the X-rays hit them perpendicularly with respect to their main axes. In Figure 1b the result of such a stamping procedure (in this case on glass) is shown, and Figure 1c shows the stitched image of a complete Si_3N_4 window created from fluorescence micrographs of different regions of the window.

Immediately after stamping, the immobilized bundles were fixed with formaldehyde, permeabilized with Triton X-100 (Carl Roth, Karlsruhe, Germany), and stained with phalloidin conjugated to AlexaFluor 594 (Invitrogen GmbH, Darmstadt, Germany). The high specificity of phalloidin to F-actin helped us to distinguish actin in stereocilia from any other cell fragment with elongated shape potentially present on the window. The AlexaFluor dyes are resistant to freeze-drying, so the presence of actin-based stereocilia on the frames can be reassessed after lyophilization to exclude loss or spatial rearrangement of stereocilia. We characterize the stereocilia by fluorescence microscopy. As examples we show in Figure 1c a stitched image of a whole Si_3N_4 window after staining and in Figure 2b,d and Figure 3a,b representations with higher magnification. During the X-ray diffraction experiments we used bright field contrast online at the beamline to identify stereocilia bundles by shape, as shown in Figure 3c.

The fixation and lyophilization procedures stabilized the samples and enabled us to obtain data from cellular structures in well-preserved structural conditions and at the same time a comparably high electron density contrast between the sample and the surrounding air. By comparing the microscopy images before and after lyophilization, we did not observe any morphological changes. However, we cannot exclude a certain degree of degradation that is possibly not detectable by visual control with the microscope. Additionally, we have shown previously that chemical fixation does indeed alter intracellular nanostructure.[28]

Ptychography and nanodiffraction are complementary X-ray techniques,[31] which are very well suited to characterize biomolecular assemblies on the relevant length scales, as they bridge μm-resolution in real-space and nm-resolution in reciprocal space. A great advantage of hard X-ray methods as compared to electron microscopy (EM), which also provides nm resolution, is the high penetration power, allowing for the study of the internal structure of samples without the need of sectioning.

Ptychography is a coherent diffraction imaging (CDI) technique in which the sample is illuminated by a confined, coherent beam at different partially overlapping positions. At each position a coherent diffraction pattern is recorded in the far field with a 2D pixel detector, and phase retrieval algorithms are then employed to retrieve the 2D complex-valued transmissivity of the specimen.[32,33] An important advantage of CDI is that lenses are not needed, which is a promising approach to achieve X-ray imaging of biological specimens with high resolution.[34] X-ray ptychography has previously been used to image freeze-dried[35,31] and frozen-hydrated[36] biological samples.

Ptychography experiments are conducted at the cSAXS beamline of the Swiss Light Source at the Paul Scherrer Institute in Villigen, Switzerland, using an

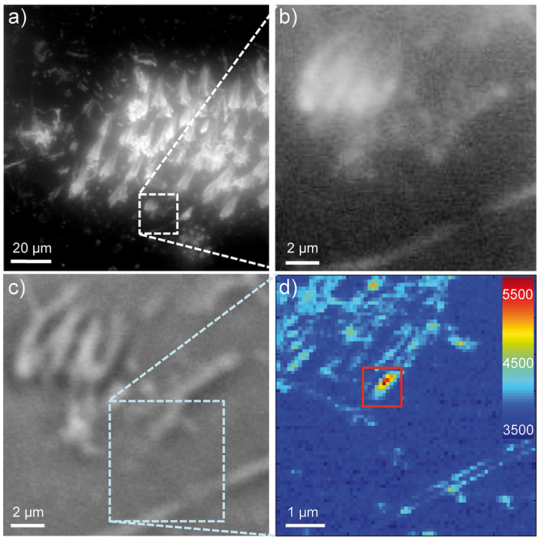

Figure 3. Scanning nanodiffraction imaging of isolated stereocilia. (a) Fluorescence micrograph recorded after freeze-drying the sample. (b) Zoom-in of the region indicated by the box in (a). (c) Image taken with the beamline microscope prior to the X-ray experiments. (d) X-ray dark field image of the region indicated by the box in (c). The step size is 100 nm. Red regions show the highest total intensity, blue the lowest (background/substrate); scale bar shows photons/s. The red box indicates the region of interest which is scanned with a smaller step size, as shown in Figures 4a,b,d,e.

energy of 8.7 keV. The beam has a size of 4.0 μm at the position of the sample and a flux of $\sim$4.2 $\times$ 10^8 photons/s. Ptychographic scans cover an area of 24 $\times$ 24 μm^2 of the specimen, and ptychographic reconstructions are performed as described in the Methods. For each image we estimate that a dose of about 5 $\times$ 10^4 Gy is imparted on the specimen. The resolution is estimated by analyzing the radially averaged power spectrum density of the images to be about 130 nm, probably limited by the dose.

In Figure 2a,c we show two examples of groups of stereocilia corresponding to regions of interest within two ptychographic images. More specifically, we show the phase of the reconstructed image, which has a low contrast, as expected for thin biological specimens. Interestingly, we can still image the corresponding positions in visible light fluorescence microscopy *after* the X-ray ptychography measurements, as shown in Figure 2b,d. This observation promotes ptychography as a real-space nanoimaging method, which introduces a low dose to the sample compared to the X-ray diffraction experiments shown below. We note that the phase in ptychographic images can be directly related to the projection of the electron density of the specimen, allowing for a quantitative interpretation of the image. This provides a complementary tool to fluorescence microscopy, where the contrast arises from fluorophores specifically attached to proteins and is therefore an indirect way of imaging. As an example, we estimate the diameter of the stereocilium marked with an orange box in Figure 2a as shown in Figure 2e even though the width of the feature is about 145 nm, only slightly larger than the estimated resolution of 130 nm. For this purpose we model a cylindrical shaped stereocilium of density 1.35 g/cm^3,[3,34] calculate its phase profile, and convolute it with a point spread function modeled by a sinc function of 130 nm width. The choice of point spread function is justified because in CDI the detector serves as the entrance pupil and it has a square shape, which corresponds to a sinc point spread function. By fitting this model to the data, considering both the height and the width of the measured profile, we obtain a sample diameter of 100 nm. Whereas this value lies below the value expected from the analysis of electron micrographs, we note here that in both cases sample preparation could influence the absolute length scales observed. In particular, in the case of our experiments, the freeze-drying process which dehydrates the samples might lead to shrinkage. However, the measured diameter lies in the expected range of a few 10s to 100s of nanometers. Comparing ptychography and visible light fluorescence microscopy, we observe much more detail for ptychography, including overlapping of individual stereocilia.

X-ray nanodiffraction measurements at EH3 of ID13 at ESRF (European Synchrotron Radiation Facility), Grenoble, France, were carried out in transmission geometry at a photon energy of 15.25 keV. The beam was focused to 125 $\times$ 200 nm^2 (h $\times$ v) using a crossed nanofocusing refractive lens system, yielding a flux of $\sim$3 $\times$ 10^9 photons/s.[22,24,26] The samples were positioned in the focus of the beam. Figure 3d shows a dark field image of a coarse mesh-scan with a step size of 100 nm and exposure time of 1 s per scan point, taken over a sample area of 7 $\times$ 7 μm^2. The diffraction data were analyzed with self-written software tools.[26−28] The dark field representation shows the integrated scattered intensity and therefore the amount of biological material with nanometer features below 38.1 nm as spatially distributed in real-space at a resolution corresponding to the beam size. Note that in this case the dark field contrast does not provide quantitative information. The overview scans help to identify certain regions of interest (ROI) and assign them to the corresponding fluorescence micrographs. The ROIs are imaged with a smaller step size of 50 nm, with 10 s exposure times (Figure 4a).

The stereocilia bundle can clearly be distinguished from the background despite the small amount of weakly scattering material. A composite image of the diffraction patterns corresponding to each position of the scan (Figure 4b) shows a high degree of orientation, indicating the presence of highly ordered structures which by phalloidin staining can be identified as actin inside the auditory stereocilia. Overlaid with the dark field image in Figure 4a are the direction and the degree of orientation in each scan point. For this

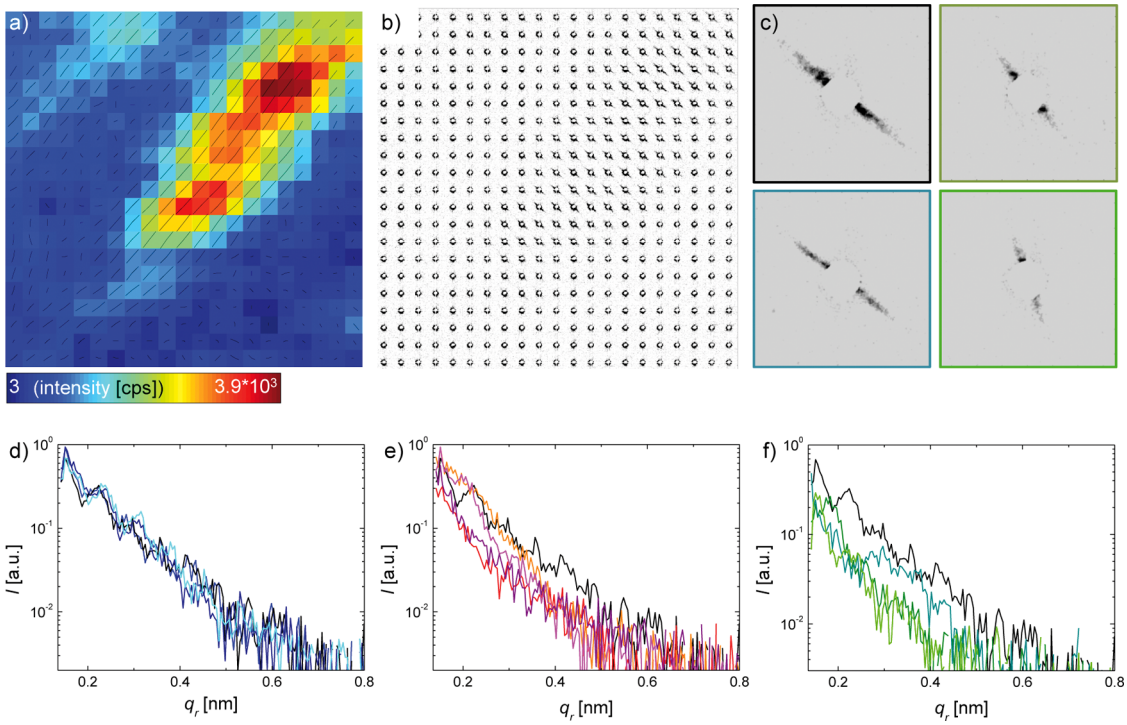

Figure 4. Analysis of diffraction patterns. (a) Dark field image overlaid with black lines indicating the orientation and degree of ordering of the structure in the sample. This area corresponds to the region indicated by a red square in Figure 3d. The step size is 50 × 50 nm^2. (b) Composite image of the individual SAXS patterns in each scanned pixel. The direct beam is covered by a beam stop. (c) Examples of individual diffraction patterns from different samples and positions on the samples corresponding to the radial intensity profiles shown in (f). (d–f) 1D radial intensity profiles of the SAXS patterns averaged over the two out of eight angular segments aligned with the orientation of the pattern. (d) Adjacent positions on the same stereocilia bundle. (e) Separate (approximately 150 nm) positions on the same stereocilia bundle. (f) Positions on different stereocilia bundles and (bright green) on a different sample.

analysis, an ellipse is fitted to each individual diffraction pattern and the direction of the major axis and the eccentricity of the ellipse are determined.[26] In the plot, the actual direction of the structure in real-space is shown, which is perpendicular to the major axis of the scattering signal in reciprocal space. The length of the lines indicates the degree of orientations, corresponding to the eccentricity of the ellipses. The resulting plot is comparable to a director field of, *e.g.*, a liquid crystal and provides a very intuitive way of illustrating the local ordering within the sample. While the Si_3N_4 window in the background (blue) shows weak total scattering and negligible and random orientation, the signal of the stereocilia shows the expected orientation, which corresponds to the orientation of the actin filaments inside the bundles, *i.e.*, parallel to the bundles. Comparing this signal to a previous study on intracellular keratin bundles,[26] the degree of orientation is even stronger, emphasizing the extremely pronounced order and paracrystalline nature.

In Figure 4c, we show examples of individual diffraction patterns. The locally different structure, *i.e.*, angle of oriented signal, degree of orientation, occurrence of modulation in the signal, and overall strength of the signal, can clearly be observed. The individual diffraction patterns provide even more information contained in the radial intensity distribution. We perform azimuthal integration on selected representative diffraction patterns to obtain the intensity distribution versus the scattering vector q_r. As shown in Figure 4a–c, the scattering intensity is highly anisotropic. We therefore divide the pattern into eight angular segments, azimuthally integrate the intensity, and average those two segments that are in line with the major axis of the fitted ellipse.[26] The number of eight segments was determined because splitting the signal into more segments does not provide additional information (but lower signal-to-noise), whereas fewer segments lead to smearing-out of the signal. Parts d–f of Figure 4 show three different groups of such $I(q_r)$ curves: (d) from positions at most 150 nm apart on the same stereocilia bundle; (e) from positions more than 150 nm apart on the same stereocilia bundle; and (f) from positions on different stereocilia bundles and even on different samples/preparations. We observe that the structure depends highly on the position. Adjacent positions lead to very similar X-ray signals, including peaks at almost identical positions. When comparing positions with a distance of more than 150 nm, the individual curves differ considerably, emphasizing the need for high real-space resolution (*i.e.*, beam diameter and step size) for these studies. In fact, the difference between these curves (shades of red, Figure 4e) is similar to the ones for different

bundles (shades of green, Figure 4f), confirming the reproducibility of the sample preparation and data acquisition. At the same time, however, we clearly observe a pronounced heterogeneity even within one bundle.

This result demonstrates the strength of the employed high-resolution technique that can access the local, internal nanostructure by scanning the sample through the beam. X-ray nanodiffraction provides real-space resolution on the order of the beam size combined with higher resolution on the nanoscale, as defined by the accessible q-range in reciprocal space. In Figure 4d−f we show the signal up to $q_r = 0.8\ \mathrm{nm}^{-1}$, corresponding to $d = 2\pi/q_r = 7.9$ nm, and therefore on the order of the diameter of the actin filaments. Higher q_r values are not shown due to dominating noise in the data. The length scales in the system are comparable to this reciprocal space resolution limit; in real space, the beamsize is $125 \times 200\ \mathrm{nm}^2$ and the diameter of one stereocilium is roughly 250 nm (see Figure 1e for a size comparison of the investigated structure and the beam size). From EM images we estimate the spacing between the filaments within a bundle to be about 10 nm, thus leaving a bit of space between the 7 nm diameter actin filaments. Therefore, perpendicular to the longitudinal direction of the filaments, we capture 15−20 repeat units, *i.e.*, individual filaments, by the X-ray beam. By contrast, along the longitudinal axis of the filaments, the helical pitch of 72 nm leads to only two to three repeat units, *i.e.*, helical turns, within the size of the beam. The latter situation is very likely the reason why—in contrast to data from *in vitro* experiments with larger beams[19−21]—we do not observe a scattering signal from the 13/6 geometry of the actin filaments. Note, however, that the sample preparation for EM as well as for our experiments can lead to changes on these length scales.

The observed heterogeneity within the signal from one bundle and between several bundles is not necessarily in contradiction with the requirement for identical thickness and build-up for all stereocilia of the same type to be reliable sensors for proprioception and hearing. Given the tiny probe volume, the usual "powder-averaging" as known from *in vitro* experiments where every possible orientation of the randomly distributed crystalline or liquid-crystalline domains is captured by a rather large X-ray beam cannot be applied here. Consequently, our diffraction signals do show peaks, but indexing them unambiguously is not possible in a straightforward way. From EM studies[3] we assume the individual filaments in the bundle to be oriented in a hexagonal array with short-range order. The sample preparation method ensures that the bundles lie flat on the substrate, but we cannot control the rotation around the long axis of the filament, *i.e.*, the angle γ in Figure 1e. Moreover, a small rotation of the sample plane around both directions defining this plane, which are the angles α and β in Figure 1e, is inevitable as we place the sample into the setup by hand. This circumstance leads to a tilt of the lattice planes of the hexagonal filament assembly with respect to the incoming X-rays.

The existence of peaks in different scan positions, reproducibly for different samples, points at a highly ordered structure. From comparison to visible light microscopy images, we can correlate the strongly anisotropic signal to the orientation perpendicular to the filament. In analogy to diffraction on gratings this signal corresponds to a characteristic length scale in the orientation perpendicular to the filament axis. We see no considerable signal perpendicular to this primary orientation, for reasons explained above.

Alternatively to a structure factor, the modulation in the signal could also stem from the form factor of characteristic features in the sample. Fitting the form factor of a cylinder to the data we obtain a diameter of 75 nm, corresponding well to the diameter value of 100 nm we obtain from the ptychography data. The same length scale is reflected in the peak width Δq, which provides information about the grain or domain size Δd involved. In the example in Figure 4d, $\Delta q \approx 0.1\ \mathrm{nm}^{-1}$, so $\Delta d = 2\pi/\Delta q \approx 62$ nm.

In the X-ray nanodiffraction experiment we estimate that doses of 1.1×10^8 Gy and 4.4×10^9 Gy are imparted to the specimen for the overview scan in Figure 3d and for the scan in Figure 4a, respectively, which are several orders of magnitude higher than the dose estimated for the ptychographic images in Figure 2a,c. This is not surprising given the fact that in the X-ray nanodiffraction experiment we gain information about nanoscale features down to 7 nm, while the X-ray ptychography experiment has a resolution of 130 nm. According to ref 34, the maximum tolerable dose for imaging with X-rays at a resolution of 7 nm is 10^9 Gy. However, in the current X-ray nanodiffraction experiment we only detect signal up to this length scale, for which it is possible that the sample tolerates a higher dose.

CONCLUSIONS

We demonstrate that hair cell stereocilia bundles can be directly imaged by X-ray ptychography and structural information in reciprocal space can be obtained by scanning X-ray nanodiffraction. The complementary X-ray methods are applied to carefully prepared samples of intact strerocilia taking into account the high complexity of any biological system as compared to purified *in vitro* systems.

We make use of the ability of X-rays to probe micrometer-thick samples and thus provide structural information and quantitative phase contrast from within the stereocilia without the need for sectioning or labeling. Thus, the presented combination of X-ray techniques provides a very suitable complement to high resolution real-space techniques such as EM or

atomic force microscopy which are used to image the surface of the sample. The study of freeze-dried samples is a necessary first step toward investigating hydrated, unfixed cellular samples by X-rays.

The use of a small X-ray beam probing a small sample volume enables us to classify and quantify the *local*, *internal* structure including direction and degree of orientation and characteristic length scales of the nanoscale biomolecular assemblies at high spatial resolution on the order of 100 nm in real-space and down to about 7 nm in reciprocal space. An important conclusion is that the nanoscale structure of the system shows considerable heterogeneity on real-space distances of about 150 nm, approximately corresponding to the diameter of one stereocilium, as well as between different bundles. This heterogeneity may include translational as well as rotational contributions. Techniques like TEM have displayed an apparently even distribution of filaments inside stereocilia, but the β and γ isoforms of actin, which have both been detected in stereocilia,[37−39] could potentially generate local heterogeneities inside stereocilia. Such heterogeneities could be due to differences in isoform appearance time, single filament geometry, twist, differential association with ABPs or ions, and cofactors.[40,41]

X-ray nanodiffraction now permits the study of native, noncrystallized biological systems with unprecedented structural resolution without averaging out such heterogeneities. From a biological point of view, the extremely pronounced anisotropy of the individual scattering patterns and distinctness of the peaks in the 1D radial intensity profiles are of interest as these features are more pronounced than for, *e.g.*, intracellular keratin bundles, which we previously studied in a comparable setting.[26] This finding stresses hair cell stereocilia as a prime example of biomolecular self-assembly showing an exceptional order and degree of orientation of individual actin filaments inside the stereocilia, reflecting their function in the organism to act as a mechanical force sensor.

X-ray ptychography quantitatively visualizes stereocilia bundles in phase contrast without any prior labeling or staining procedures. Thus, as compared to EM or fluorescence microscopy, we employ a *direct* imaging method and therefore determine the geometry of the individual stereocilia. This structural information could become even more informative in 3D by acquiring 2D projection images at different incident angles and reconstructing the 3D electron density of the sample with tomographic reconstruction methods.

Thanks to the high structural resolution, X-rays could potentially also be employed to detect changes in stereocilia structure caused by noise damage. Furthermore, measurements on fresh, unfixed stereocilia may provide additional information about the molecular composition of rootlets and the spatial distribution of populations of filaments inside them.[42,43] Apart from these sample-specific results on a highly relevant biological system, our study demonstrates the potential of the presented high-resolution X-ray techniques to be applied to many other biological and soft matter systems while maintaining an acceptable level of sample integrity throughout preparation. We therefore foresee that these complementary techniques will bring new insights concerning biological systems while disturbing the native structure and assembly as little as possible.

METHODS

Blotting of Stereocilia. Dissection of P4 (postnatal day 4) mouse ears was performed under a stereo-microscope (Olympus, Hamburg, Germany) in cold saline solution (HBSS, Hank's Balanced Salt Solution, Sigma-Aldrich, München, Germany) buffered with 10 mM HEPES to pH 7.4. The apical surfaces of the vestibular sensory epithelia were exposed by mechanical removal of the otolithic membrane after 5 min incubation in 0.1 mg/mL protease XXIV (Sigma-Aldrich). After removal of the utricle, its stereocilia were isolated by blotting the whole tissue gently onto 5 × 5 mm^2 Si_3N_4 frames with a membrane size of 0.25 × 0.25 mm^2 and 1 μm thickness (Silson Ltd., Blisworth, England). The frames had been previously coated for 20−40 min with poly-L-ornithine (Sigma-Aldrich; 0.1 mg/mL in H_2O) on the etched side of the frame to promote adhesion of the stereocilia (see Figure 1a). For test purposes and to obtain optimal imaging properties, stereocilia were also blotted on glass coverslips cleaned with 70% ethanol and by plasma treatment for several minutes. All experiments complied with national animal care guidelines and were approved by the University of Göttingen board for animal welfare and the animal welfare office of the state of Lower Saxony.

Staining of Stereocilia. Isolated stereocilia were fixed in 4% formaldehyde solution in HBSS at room temperature, rinsed with HBSS, and stained with AlexaFluor 564-phalloidin (Invitrogen GmbH, Darmstadt, Germany; 1 unit of 5 μL in 200 μL) in a 0.2% solution of Triton X-100 (Carl Roth, Karlsruhe, Germany) in HBSS. After 30 min staining at room temperature, stereocilia were repeatedly rinsed with abundant HBSS.

Mapping of Stereocilia. Stained stereocilia blotted on Si_3N_4 frames were successively imaged with an Olympus IX71 epifluorescence microscope (Olympus, Hamburg, Germany) equipped with a 10× and a 20× objective. The "MosaicJ" stitching plug-in of FIJI was used off-line for creating a map of the fluorescent objects in relation to the frame, with the goal of facilitating sample localization during the subsequent experiments at the synchrotron. The sample regions imaged by ptychography were additionally imaged afterward at 60× magnification using an oil immersion objective.

Freeze-Drying of the Samples. Mapped frames were then processed for lyophilization. Before plunge-freezing, the samples were briefly washed in ultrapure water to avoid excessive salt precipitation on the membrane. The freezing step was carried out with a Leica EM GP plunge freezer (Leica, Vienna, Austria). The samples were then placed in a custom-made freeze-drier and removed after approximately 40 h under vacuum (pressures ranging from 2×10^{-2} to 4×10^{-6} mbar). The temperature was then increased from −197.6 to 20 °C either by venting the samples with N_2 overnight or by letting them equilibrate slowly at room temperature.

Postlyophilization Mapping. Contrary to most genetically encoded fluorophores, AlexaFluor retains most of its fluorescence even after lyophilization. Therefore, additional micrographs of

the frames were taken to document possible stereocilia loss or morphological change during the freeze-drying steps.

X-ray Ptychography Experiments and Reconstructions. X-ray ptychography experiments were performed at the cSAXS beamline at the Swiss Light Source at the Paul Scherrer Institute in Villigen, Switzerland. The energy used was 8.7 keV, and the beam was focused by a coherently illuminated Fresnel zone plate made of Au with an outermost zone width of 100 nm and a diameter of 150 μm.[44] The sample was placed at 2.8 mm downstream of the focus, where the beam had a diameter of 4.0 μm. A Pilatus 2 M detector[45] with 172 μm pixel size, placed at 7.525 m downstream of the sample, was used to record the data. Coherent diffraction patterns were recorded at 323 positions distributed in a grid of concentric circles with a radial step of 1.2 μm, as described elsewhere,[46] and covering a field of view of 24 $\times$ 24 μm^2. We note that under these experimental conditions the beam is significantly larger than the 3.1 μm required for Nyquist sampling. However, the overlapping of the illumination on the specimen at adjacent scanning positions in our experiment, determined by a shell step size of 1.2 μm in the circular ptychographic scan, is sufficient to compensate for a sampling on the detector smaller than the Nyquist sampling, as reported in ref 47. The acquisition time at each position was 0.2 s, and each scan took 129 s including overhead time due to sample positioning with a piezoelectric stage. For sample alignment prior to the X-ray measurements, a visible light microscope was moved into the beam path. For ptychographic reconstructions 192 $\times$ 192 pixels of the detector were used, leading to a pixel size of 31.47 nm in the reconstructions. The reconstructions were performed with 10 iterations of the difference map algorithm[48,49] followed by 200 iterations of a maximum likelihood optimization algorithm.[50] For the reconstructions we used an initial probe determined from a previous ptychographic experiment with a strong scattering object consisting of a test pattern, since this has been proven to be crucial for ptychographic reconstructions of weakly scattering specimens.[46]

X-ray Nanodiffraction Experiments. X-ray nanodiffraction experiments were performed at the experimental hutch III of the beamline ID13 at the European Synchrotron Radiation Facility (ESRF, Grenoble, France). The exact setup and method used are described in detail elsewhere.[26] Briefly, an X-ray beam (photon energy 15.25 keV, flux 3 $\times$ 10^9 photons/s) was focused[22,24] to a spot size of about 200(h) $\times$ 125(v) nm^2. The sample was scanned through the beam with nanometer precision and the diffraction signal was recorded using a Maxipix detector (ESRF, Grenoble, France) at a sample-to-detector distance of about 0.9 m. For sample alignment prior to the X-ray measurements, a visible light microscope was moved into the beam path. Scanning step sizes were 100−200 nm with exposure times of 1 s per pixels for coarse overview scans and 50 nm with exposure times of 10 s per pixel for finer ROI (region of interest) scans. Total number of steps and thereby total scan time was adjusted to the size of the region to investigate. The data shown here stem from two different samples (different mice and different preparations) and from different positions on these samples. The good agreement between the results corroborates our assumption that they are sample-independent.

Data Analysis. Data analysis was performed using self-written Matlab (The Mathworks, Natick, MA) tools as described previously.[26] The data were further processed using the commercial software Origin (OriginLab, Northampton, MA).

Dose Estimation. The dose D imparted on the specimen has been estimated as $D = \mu N_0 \varepsilon/\rho$, where μ is the linear attenuation coefficient of the specimen, N_0 is the number of photons incident on the specimen per unit area, ε is the photon energy, and ρ is the mass density of the specimen, assuming that the sample is composed of a protein of empirical formula $H_{50}C_{30}N_9O_{10}S_1$ and density 1.35 g/cm^3.[34]

Conflict of Interest: The authors declare no competing financial interest.

Acknowledgment. The experiments were carried out at the beamline ID13, ESRF, Grenoble, France, and at the cSAXS beamline at the Swiss Light Source in Villigen, Switzerland. We thank T. Moser for providing the mouse samples and for fruitful discussions, J. Herbst for help with cryo-fixation and freeze-drying, D. Karavitaki for suggestions on the cilia blotting, and T. Pfohl, M. Guizar-Sicairos, A. Menzel, and T. Salditt for fruitful discussions. This work was supported by the German Research Foundation (DFG) in the framework of SFB 755 "Nanoscale Photonic Imaging", within project C10, the Cluster of Excellence and DFG Research Center "Nanoscale Microscopy and Molecular Physiology of the Brain" (CNMPB), and the Excellence Initiative. V.P. was supported by a fellowship of the Alexander von Humboldt Foundation. B.W. was supported by a fellowship of the Deutsche Telekom Stiftung. V.P. prepared the samples, performed measurements, analyzed data, and wrote the manuscript. B.W. performed measurements and analyzed data. A.D. gave support during the experiments, performed measurements, and analyzed ptychographic data. C.M. and C.D. performed measurements. M.R. and M.B. gave support and helpful advice during the measurements. S.K. designed the research, directed the project, performed measurements, analyzed data, and wrote the manuscript. All authors discussed the results and commented on the manuscript.

REFERENCES AND NOTES

1. Zhang, D.-S.; Piazza, V.; Perrin, B. J.; Rzadzinska, A. K.; Poczatek, J. C.; Wang, M.; Prosser, H. M.; Ervasti, J. M.; Corey, D. P.; Lechene, C. P. Multi-Isotope Imaging Mass Spectrometry Reveals Slow Protein Turnover in Hair-Cell Stereocilia. *Nature* **2012**, *481*, 520–524.
2. Chen, P. Y.; McKittrick, J.; Meyers, M. A. Biological Materials: Functional Adaptations and Bioinspired Designs. *Prog. Mater. Sci.* **2012**, *57*, 1492–1704.
3. Derosier, D. J.; Tilney, L. G.; Egelman, E. Actin in the Inner Ear: The Remarkable Structure of the Stereocilum. *Nature* **1980**, *287*, 291–296.
4. Huxley, H. E. Fifty Years of Muscle and the Sliding Filament Hypothesis. *Eur. J. Biochem.* **2004**, *271*, 1403–1415.
5. Huxley, H. E. X-Ray Analysis and the Problem of Muscle. *P. R. Soc. London B. Bio.* **1953**, *141*, 59–62.
6. Huxley, H. E.; Steward, A.; Sosa, H.; Irving, T. X-Ray Diffraction Measurements of the Extensibility of Actin and Myosin Filament in Contracting Muscle. *Biophys. J.* **1994**, *67*, 2411–2421.
7. Hanson, J. Evidence from Electron Microscope Studies on Actin Paracrystals concerning the Origin of the Cross-Striation in the Thin Filaments of Vertebrate Skeletal Muscle. *Proc. R. Soc. London B. Bio.* **1973**, *183*, 39–58.
8. Holmes, C. K.; Popp, D.; Gebhard, W.; Kabsch, W. Atomic Model of the Actin Filament. *Nature* **1990**, *347*, 44–49.
9. Egelman, E. H.; Orlova, A. New Insights Into Actin Filament Dynamics. *Curr. Opin. Struct. Biol.* **1995**, *5*, 172–180.
10. Wong, G. L. C.; Tang, J. X.; Lin, A.; Li, Y.; Janmey, P. A.; Safinya, C. R. Hierarchical Self-Assembly of F-Actin and Cationic Lipid Complexes: Stacked Three-Layer Tubule Networks. *Science* **2000**, *288*, 2035–2039.
11. Angelini, T. E.; Liang, H.; Wriggers, W.; Wong, G. C. L. Like-Charge Attraction Between Polyelectrolytes Induced by Counterion Charge Density Waves. *Proc. Natl. Acad. Sci. U.S.A.* **2003**, *100*, 8634–8637.
12. Sanders, L. K.; Xian, W.; Guaqueta, C.; Strohman, M. J.; Vrasich, C. R.; Luitjen, E.; Wong, G. C. L. Control of Electrostatic Interactions Between F-Actin and Genetically Modified Lysozyme in Aqueous Media. *Proc. Natl. Acad. Sci. U.S.A.* **2007**, *104*, 15994–19999.
13. Wong, G. C. L.; Pollack, L. Electrostatics of Strongly Charged Biological Polymers: Ion-Mediated Interactions and Self-Organization in Nucleic Acids and Proteins. *Annu. Rev. Phys. Chem.* **2010**, *61*, 171–189.
14. Pelletier, O.; Pokidysheva, E.; Hirst, L. S.; Bouxsein, N.; Li, Y.; Safinya, C. R. Structure of Actin Cross-Linked with α-Actinin: A Network of Bundles. *Phys. Rev. Lett.* **2003**, *91*, 148102.
15. Flock, A.; Bretscher, A.; Weber, K. Immunohistochemical Localization of Several Cytoskeletal Proteins in the Inner Ear Sensory and Supporting Cells. *Hearing Res.* **1982**, *7*, 75–89.

16. Shahin, H.; Walsh, T.; Sobe, T.; Abu Sa'ed, J.; Rayan, A. A.; Lynch, E. D.; Lee, M. K.; Avraham, K. B.; King, M. C.; Kanaan, M. Mutations in a Novel Isoform of TRIOBP That Encodes a Filamentous-Actin Binding Protein Are Responsible for DFNB28 Recessive Nonsyndromic Hearing Loss. *Am. J. Hum. Genet.* **2006**, *78*, 144–152.
17. Zheng, L.; Sekerkova, G.; Vranich, K.; Tilney, L. G.; Mugnaini, E.; Bartles, J. R. The Deaf Jerker Mouse Has a Mutation in the Gene Encoding the Espin Actin-Bundling Proteins of Hair Cell Stereocilia and Lacks Espins. *Cell* **2000**, *102*, 377–385.
18. Lieleg, O.; Schmoller, K. M.; Purdy Drew, K. R.; Claessens, M. M. A. E.; Semmrich, C.; Zheng, L.; Bartles, J. R.; Bausch, A. R. Structural and Viscoelastic Properties of Actin Networks Formed by Espin or Pathologically Relevant Espin Mutants. *ChemPhysChem* **2009**, *10*, 281–2817.
19. Purdy, K. R.; Bartles, J. R.; Wong, G. C. L. Structural Polymorphism of the Actin-Espin System: A Prototypical System of Filaments and Linkers in Stereocilia. *Phys. Rev. Lett.* **2007**, *98*, 058105.
20. Shin, H.; Purdy Drew, K. R.; Bartles, J. R.; Wong, G. C. L.; Grason, G. M. Cooperativity and Frustration in Protein-Mediated Parallel Actin Bundles. *Phys. Rev. Lett.* **2009**, *103*, 238102.
21. Claessens, M. M. A. E.; Semmrich, C.; Ramos, L.; Bausch, A. R. Helical Twist Controls the Thickness of F-Actin Bundles. *Proc. Natl. Acad. Sci. U.S.A.* **2008**, *105*, 8819–8822.
22. Schroer, C. G.; Kuhlmann, M.; Hunger, U. T.; Günzler, T. F.; Kurapova, O.; Feste, S.; Frehse, F.; Lengeler, B.; Drakopoulos, B.; Somogyi, A.; Simionovici, A. S.; Snigirev, A.; Snigireva, I.; Schug, C.; Schröder, W. H. Nanofocusing Parabolic Refractive X-ray Lenses. *Appl. Phys. Lett.* **2003**, *82*, 1485–1487.
23. Schropp, A.; Boye, P.; Feldkamp, J. M.; Hoppe, R.; Patommel, J.; Samberg, D.; Stephan, S.; Giewekemeyer, K.; Wilke, R. N.; Salditt, T.; Gulden, J.; Mancuso, A. P.; Vartanyants, I. A.; Weckert, E.; Schöder, S.; Burghammer, M.; Schroer, C. G. Hard X-Ray Nanobeam Characterization by Coherent Diffraction Microscopy. *Appl. Phys. Lett.* **2010**, *96*, 091102.
24. Schroer, C. G.; Kurapova, O.; Patommel, J.; Boye, P.; Feldkamp, J.; Lengeler, B.; Burghammer, M.; Riekel, C.; Vincze, L.; van der Hart, A.; Küchler, M. Hard X-Ray Nanoprobe Based on Refractive X-Ray Lenses. *Appl. Phys. Lett.* **2005**, *87*, 124103.
25. Sedlmair, J.; Gleber, S.-C.; Öztürk-Mert, S.; Bertilson, M.; von Hofsten, O.; Thieme, J.; Pfohl, T. Imaging of Vascular Smooth Muscle Cells with Soft X-Ray Spectromicroscopy. *Microsc. Microanal.* **2011**, *17*, 991–1001.
26. Weinhausen, B.; Nolting, J.-F.; Olendrowitz, C.; Langfahl-Klabes, J.; Reynolds, M.; Salditt, T.; Köster, S. X-Ray Nano-Diffraction on Cytoskeletal Networks. *New J. Phys.* **2012**, *14*, 085013.
27. Weinhausen, B.; Köster, S. Microfluidic Devices for X-ray Studies on Hydrated Cells. *Lab Chip* **2012**, *13*, 212–215.
28. Weinhausen, B.; Saldanha, O.; Wilke, R. N.; Dammann, C.; Priebe, M.; Burghammer, M.; Sprung, M.; Köster, S. Scanning X-Ray Nanodiffraction on Living Eukaryotic Cells in Microfluidic Environments. *Phys. Rev. Lett.* **2014**, *12*, 088102.
29. Alberts, B.; Johnson, A.; Raff, M.; Roberts, K.; Walter, P. In *The Molecular Biology of the Cell*; Taylor and Francis/Garland Science: New York, 2001.
30. Rusch, A.; Eatock, R. A. A Delayed Rectifier Conductance in Type I Hair Cells of the Mouse Utricle. *J. Neurophysiol.* **1996**, *76*, 995–1004.
31. Wilke, R. N.; Priebe, M.; Bartels, M.; Giewekemeyer, K.; Diaz, A.; Karvinen, P.; Salditt, T. Hard X-ray Imaging of Bacterial Cells: Nano-Diffraction and Ptychographic Reconstruction. *Opt. Express* **2012**, *20*, 19232–19254.
32. Faulkner, H. L. M.; Rodenburg, J. M. Movable Aperture Lensless Transmission Microscopy. *Phys. Rev. Lett.* **2004**, *93*, 023903.
33. Rodenburg, J. M.; Huerst, A. C.; Cullis, A. G.; Dobson, B. R.; Pfeiffer, F.; Bunk, O.; David, C.; Jefimovs, K.; Johnson, I. Hard-X-ray Lensless Imaging of Extended Objects. *Phys. Rev. Lett.* **2007**, *98*, 034801.
34. Howells, M. R.; Beetz, T.; Chapman, H. N.; Cui, C.; Holton, J. M.; Jacobsen, C. J.; Kirz, J.; Lima, E.; Marchesini, S.; Miao, H.; Sayreb, D.; Shapiroa, D. A.; Spencea, J. C. H.; Starodube, D. An Assessment of the Resolution Limitation due to Radiation-Damage in X-ray Diffraction Microscopy. *J. Electron Spectrosc.* **2009**, *170*, 4–12.
35. Giewekemeyer, K.; Thibault, P.; Kalbfleisch, S.; Beerlink, A.; Kewish, C. M.; Dierolf, M.; Pfeiffer, F.; Salditt, T. Quantitative Biological Imaging by Ptychographic X-Ray Diffraction Microscopy. *Proc. Natl. Acad. Sci. U.S.A.* **2010**, *107*, 529–534.
36. Lima, E.; Diaz, A.; Guizar-Sicairos, M.; Gorelick, S.; Pernot, P.; Schleier, T.; Menzel, A. Cryo-Scanning X-Ray Diffraction Microscopy of Frozen-Hydrated Yeast. *J. Microsc.* **2013**, *249*, 1–7.
37. Hofer, D.; Ness, W.; Drenckhahn, D. Sorting of Actin Isoforms in Chicken Auditory Hair Cells. *J. Cell Sci.* **1997**, *110*, 765–770.
38. Furness, D. N.; Katori, Y.; Mahendrasingam, S.; Hackney, C. M. Differential Distribution of Beta- and Gamma-Actin in Guinea-Pig Cochlear Sensory and Supporting Cells. *Hearing Res.* **2005**, *207*, 22–34.
39. Perrin, B. J.; Sonnemann, K. J.; Ervasti, J. M. β-Actin and γ-Actin are Each Dispensable for Auditory Hair Cell Development but Required for Stereocilia Maintenance. *PLoS Genet.* **2010**, *6*, 1001158.
40. McGough, A.; Pope, B.; Chiu, W.; Weeds, A. Cofilin Changes the Twist of F-Actin: Implications for Actin Filament Dynamics and Cellular Function. *J. Cell Biol.* **1997**, *138*, 771–781.
41. Galkin, V. E.; Orlova, A.; Lukoyanova, N.; Wriggers, W.; Egelman, E. H. Actin Depolymerizing Factor Stabilizes an Existing State of F-Actin and can Change the Tilt of F-Actin Subunits. *J. Cell Biol.* **2001**, *153*, 75–86.
42. Liberman, M. C. Chronic Ultrastructural Changes in Acoustic Trauma: Serial-Section Reconstruction of Stereocilia and Cuticular Plates. *Hearing Res.* **1987**, *26*, 65–88.
43. Furness, D. N.; Mahendrasingam, S.; Ohashi, M.; Fettiplace, R.; Hackney, C. M. The Dimensions and Composition of Stereociliary Rootlets in Mammalian Cochlear Hair Cells: Comparison Between High- and Low-Frequency Cells and Evidence for a Connection to the Lateral Membrane. *J. Neurosci.* **2008**, *28*, 6342–53.
44. Gorelick, S.; Guzenko, V. A.; Vila-Comamala, J.; David, C. Direct e-Beam Writing of Dense and High Aspect Ratio Nanostructures in Thick Layers of PMMA for Electroplating. *Nanotechnology* **2010**, *21*, 295303.
45. Henrich, B.; Bergamaschi, A.; Broennimann, C.; Dinapoli, R.; Eikenberry, E. F.; Johnson, I.; Kobas, M.; Kraft, P.; Mozzanica, A.; Schmitt, B. PILATUS: A Single Photon Counting Pixel Detector for X-Ray Applications. *Nucl. Instrum. Meth. A* **2009**, *607*, 247–249.
46. Dierolf, M.; Thibault, P.; Menzel, A.; Kewish, C. M.; Jefimovs, K.; Schlichting, I.; von König, K.; Bunk, O.; Pfeiffer, F. Ptychographic Coherent Diffractive Imaging of Weakly Scattering Specimens. *New J. Phys.* **2010**, *12*, 035017.
47. Edo, T. B.; Batey, D. J.; Maiden, A. M.; Rau, C.; Wagner, U.; Pešić, Z. D.; Waigh, T. A.; Rodenburg, J. M. Sampling in X-Ray Ptychography. *Phys. Rev. A* **2013**, *87*, 053850.
48. Thibault, P.; Dierolf, M.; Menzel, A.; Bunk, O.; David, C.; Pfeiffer, F. High-Resolution Scanning X-ray Diffraction Microscopy. *Science* **2008**, *321*, 379–382.
49. Thibault, P.; Dierolf, M.; Bunk, O.; Menzel, A.; Pfeiffer, F. Probe Retrieval in Ptychographic Coherent Diffractive Imaging. *Ultramicroscopy* **2009**, *109*, 338–343.
50. Thibault, P.; Guizar-Sicairos, M. Maximum-Likelihood Refinement for Coherent Diffraction Imaging. *New J. Phys.* **2012**, *14*, 063004.